

Article

Mechanics-Seepage Experimental and Simulation Study of Gas-Bearing Coal under Different Load Paths

Haibo Sun ^{1,2,*}, Baoyong Zhang ¹, Zhijun Song ¹, Bin Shen ¹  and Hongyu Song ¹¹ School of Safety Engineering, Heilongjiang University of Science and Technology, Harbin 150022, China² Heilongjiang Longmei Jixi Mining Co., Ltd., Jixi 158199, China

* Correspondence: shbbs_hlj@163.com

Abstract: Mechanics-seepage synchronous tests on gas-bearing coal under three different stress paths were designed and implemented to evaluate how load path affected the mechanical strength and permeability of deep mining-disturbed coal. The cracks-count evolution of coal specimens during instability was observed through DEM numerical simulation. The results showed significant stress-strain and strength variations under different paths. At the time of failure, the specimen deformation and peak strength were Test 1 > Test 2 > Test 3, while the permeability was Test 3 > Test 2 > Test 1, with specimen permeability in Test 3 rising prominently. From numerical simulation, the cracks count was Test 2 > Test 3 > Test 1, with tensile cracks taking the largest proportion in Test 2 and shear cracks taking the largest proportion in Test 3. Our findings shed some light on the research and disaster prevention regarding coal and gas outburst.

Keywords: triaxial; permeability; strain; DEM; crack



Citation: Sun, H.; Zhang, B.; Song, Z.; Shen, B.; Song, H. Mechanics-Seepage Experimental and Simulation Study of Gas-Bearing Coal under Different Load Paths. *Processes* **2022**, *10*, 2255. <https://doi.org/10.3390/pr10112255>

Academic Editors: Feng Du, Aitao Zhou and Bo Li

Received: 9 October 2022

Accepted: 31 October 2022

Published: 2 November 2022

Publisher's Note: MDPI stays neutral with regard to jurisdictional claims in published maps and institutional affiliations.



Copyright: © 2022 by the authors. Licensee MDPI, Basel, Switzerland. This article is an open access article distributed under the terms and conditions of the Creative Commons Attribution (CC BY) license (<https://creativecommons.org/licenses/by/4.0/>).

1. Introduction

Coal and gas outburst, as a major cause of gas hazards in coal mines, results from a very complex dynamic instability process at underground mine sites [1,2]. When such a hazard occurs, the gas adsorption/desorption and seam stress-strain at the outburst site undergo tremendous change. The gas also affects the deformed coal body, causing it to change further [3–5]. Currently, the mechanisms underlying coal and gas outburst remain unsolved. Wider investigation into the mechanical properties and seepage behavior of gas-bearing coal under stress-seepage coupling is of great importance.

As field testing is impractical, given the high risk factor of seams prone to coal and gas outburst, experimental study of coal-gas coupling mechanisms forms the fundamental means of understanding coal permeability evolution and damage mechanisms [6,7]. Xu et al. [8,9] experimentally characterized coal deformation and permeability under loading/unloading conditions and revealed that coal permeability variation is closely related to coal deformation and damage. Yin et al. [10] evaluated the effect of loading/unloading conditions on the mechanical properties of gas-bearing coal and established a whole process seepage speed–axial pressure equation. Wang et al. [11] studied the dynamic behaviors in coal seams under different mining layouts. Zhao et al. and Wang et al. [12,13] analyzed the relationship between coal permeability, stress difference and strain during loading/unloading through whole-process stress-strain permeability tests. Li et al. [14] observed the deformation and permeability behaviors of outburst coal samples under cyclic loads and found that permeability variation is closely related to coal damage and deformation. Cao et al. [15] analyzed how confining pressure and axial pressure affect coal gas seepage under constant gas pressure. Xue et al. [16] performed uniaxial tension and compression, conventional triaxial and dynamics tests, and obtained the mechanical characteristic parameters and deformation failure behaviors of coal samples under different load paths and load rates.

The discrete element method (DEM) is an important numerical method of solving coal mechanical problems due to its ability to assess coal mechanics and crack mechanisms from a mesoscopic perspective [17–19]. Indraratna et al. [20] made cyclic biaxial simulation tests at different frequencies with DEM software. They also analyzed the evolution of meso-mechanical parameters such as contact force and bond force formed during cyclic loading and explained the mechanism of particle fracture. Wang et al. [21] simulated crack propagation with a PFC-based particle flow model and observed how coal stress affects crack propagation. Jiang et al. [22] simulated a series of biaxial compression tests with DEM and observed the mechanical behavior of deep-sea methane-hydrate-bearing soils. Ismail et al. [23] built a DEM model for visualizing damage evolution and predicting failure envelopes of composite laminae under biaxial loads. Yang et al. [24] numerically simulated the failure behavior around a circular opening under biaxial compression. Sagong et al. [25] made experimental and numerical analyses of the sliding of fissures and joints in fissure-bearing rock under biaxial compression. Raisianzadeh et al. [26] used DEM to simulate the interaction between particles under biaxial load, and studied the crack propagation path and failure strength of rock containing prefabricated cracks. Xu et al. [27] studied the influence of the angle between two cracks on the strength and crack propagation of the specimen.

From the literature review above, both physical experiments and numerical simulations help to understand the mechanisms behind coal and gas outburst. However, few attempts have been made to combine physical experiments with numerical simulation. In this paper, the deformation failure and gas-seepage behavior of briquette specimens under different stress paths are tested. The test results are then verified through particle flow code (PFC) numerical simulation. Specimen-crack evolution under different paths is also characterized. Our method offers a new approach to understanding the mechanisms behind coal and gas outburst.

2. Experimental Section

2.1. Specimen Procurement and Preparation

The structural complexity of raw coal can give rise to substantial discreteness of test results. Previous studies have demonstrated that briquette, in one way or another, possesses the physical–mechanical and adsorption properties of raw coal. It is also easy to transport and handle. For this reason, briquette is often used in laboratory studies as a substitute for raw coal [28].

The coal sample came from Jixi Mining Group's Xinfra coal mine, which is a high-gas mine. The sample has an ash content of 61.28%, a volatile content of 22.9%, and a solidity factor of 0.5866. After the sample was recovered from the mine face, it was sealed and delivered to the laboratory where it was crushed. When preparing specimens, 30 g river sand, 30 g cement, 210 g crushed coal, and 30 g water were mixed together and kept under 200 kN moulding pressure for 12 h before the specimens were demoulded and placed in a curing box for further use. Figure 1 shows the ready-made briquette specimens.

2.2. Experimental Apparatus

A triaxial servo-controlled seepage apparatus for thermofluid–solid coupling of gas-bearing coal shown in Figure 2 was used for the test, featuring $\phi 50 \text{ mm} \times 100 \text{ mm}$ standard specimens [9].

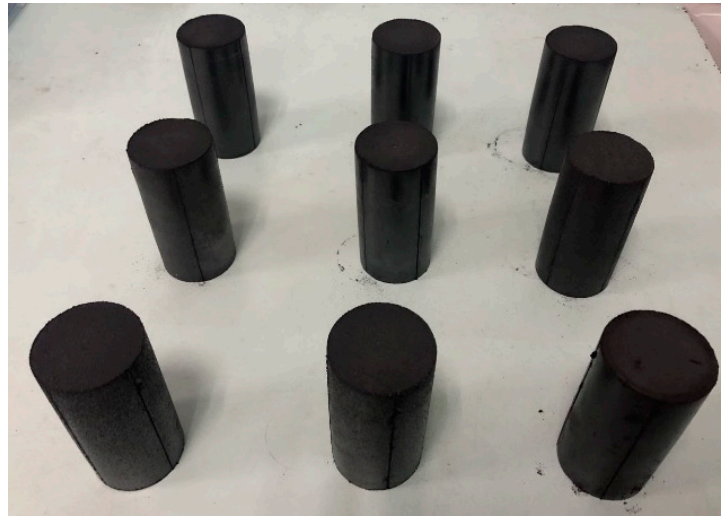


Figure 1. Briquette specimens.



Figure 2. The triaxial servo-controlled seepage equipment for thermofluid–solid coupling of coal containing methane.

2.3. Experimental Methods

The real load state of mining-disturbed coal at deep levels was simplified into three load paths: axial pressure loading in Test 1, confining pressure unloading in Test 2, and composite loading/unloading in Test 3, as shown in Figure 3, where σ_1 represents axial pressure and σ_3 represents confining pressure, and the flow chart for the experiment is shown in Figure 4. The exact test plan is described below:

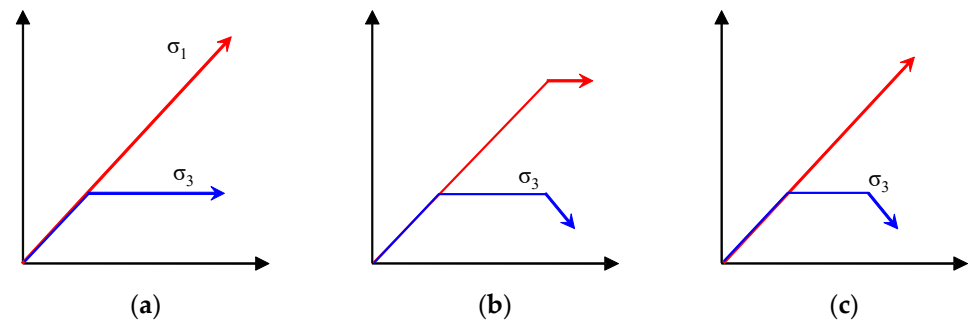


Figure 3. Schematic diagram of experimental loading path. (a) Test 1, (b) Test 2, (c) Test 3.

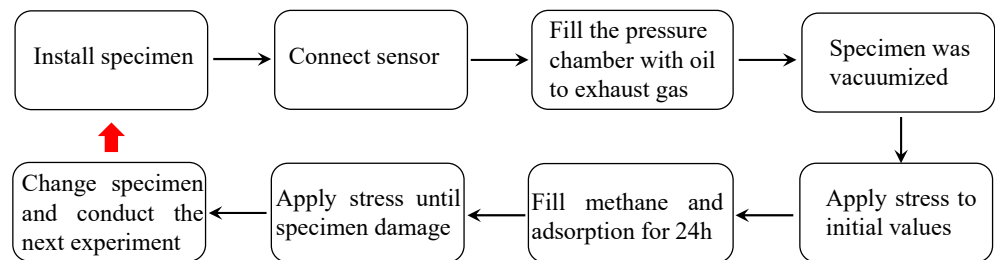


Figure 4. Flow chart for the experiment.

Test 1: Load σ_1 and σ_3 to 6 MPa, then feed 1 MPa gas. After adsorption for 24 h, load σ_1 at the rate of 5 kN/s until the specimen fails. Conduct gas seepage test at the same time.

Test 2: Load σ_1 and σ_3 to 6 MPa, then feed 1 MPa gas. After adsorption for 24 h, load σ_1 to σ_U (which is 60% of the peak axial stress in Test 1) at the rate of 5 kN/s, keep σ_1 unchanged and unload σ_3 at the rate of 0.01 mm/min until the specimen fails. Conduct gas seepage test at the same time.

Test 3: Load σ_U in the same steps as Test 2, then keep the loading rate of σ_1 unchanged and unload σ_3 at the rate of 0.01 mm/min until the specimen fails. Conduct gas seepage test at the same time.

3. Results and Analysis

3.1. Strain and Strength Characteristics

Figure 5 compares the stress-strain relationship of specimens under the true-triaxial path, where ε_1 and ε_3 are the axial strain and radial strain of the specimen, and $\Delta\sigma$ is the principal stress difference, i.e., $\sigma_1 - \sigma_3$. From these diagrams, the stress-strain curves of gas-bearing coal are much the same under the three paths. They all involve five stages: compaction, linear elasticity, plastic deformation, stress decline, and residual stress. Stress path is shown to have a strong impact on the deformation and strength of gas-bearing coal. In Test 1, the specimen strength is the highest, with stress difference of 33.750 MPa. In Test 2, the specimen strength is the second highest, with stress difference of 23.480 MPa. In Test 3, the specimen strength is the lowest, with stress difference of 16.711 MPa. The specimen-bearing capacity is greatly reduced.

At peak strength, ε_1 and ε_3 are 2.607 and -1.771 in Test 1; 1.301 and -1.354 in Test 2; and 0.793 and -2.186 in Test 3. In Test 1, the axial strain is the largest. In Test 3, the axial strain is the smallest, but the radial strain is the largest. At peak strength, the axial-to-radial strain ratios of the specimens are 1.472, 0.961, and 0.363. The gradual reduction in the axial-to-radial strain ratio indicates that, during instability, the axial deformation intensifies and the specimen is more prone to axial failure, especially in Test 3, where the specimen has a strong shear dilatancy. Also, by observing the stress-strain curves, it can be seen that the post-peak curve slope gradually increases. In Test 2 and Test 3, with the unloading of confining pressure, the strain increment gradually increases. When this increase has accumulated to a limit, the bearing capacity declines and the specimen

immediately becomes unstable. This is particularly obvious in Test 3, where the specimen gradually changes from ductile failure to brittle failure.

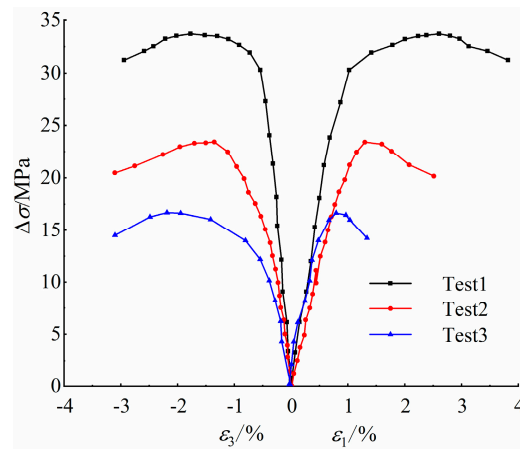


Figure 5. Stress–strain curves of specimens under different test paths.

3.2. Permeability Evolution Characteristics

Gas seepage in the specimens obeys Darcy's law. Permeability is calculated by the following formula [29]:

$$K = \frac{2P_0'QL\mu}{A(P_1^2 - P_2^2)} \quad (1)$$

where K is permeability (m^2); Q is the gas flow (m^3/s); μ is the absolute viscosity of the methane; L is the specimen length (m); A is the effective area of permeability (m^2); P_0' is standard atmosphere; P_1 is the inlet pressure (MPa); and P_2 is outlet pressure (MPa).

Figure 6 compares the principal stress difference and permeability variations of gas-bearing coal as a function of axial strain under different test paths. From the $\varepsilon_1-\Delta\sigma$ and ε_1-K curves, as the test goes on, permeability first reduces then increases; the valley deflection of permeability falls before the peak deflection of the $\varepsilon_1-\Delta\sigma$ curve in all cases. This is because, during elastic deformation at the beginning of the test, with the loading of external stress, the primary pores and fissures inside the specimen are compressed, which narrows the gas seepage pathway and brings down the permeability. With the loading of σ_1 , the specimen enters plastic deformation. Cracks begin to develop inside and damage is expanded, adding more seepage pathways and stepping up permeability. After that, with the further increase of σ_1 , cracks inside become interconnected, leading to instability failure. The gas seepage pathway is opened and the permeability soars.

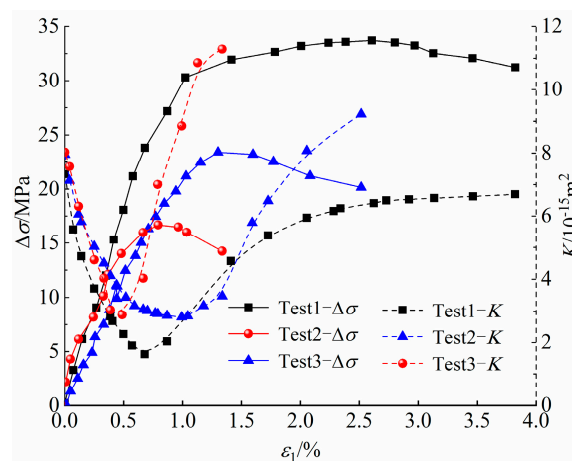


Figure 6. Variation curves of principal stress difference and permeability with axial strain during test.

Relative permeability (w) variations were observed against initial permeability to examine how stress path affects permeability evolution. From the diagram in Figure 7, under Test 1, the specimen permeability variation is modest, with minimum w of 0.222, which increases marginally to 0.913 at the end of the test. Under Test 2, w is 0.353 minimum and 0.358 maximum. Under Test 3, w is 0.370 minimum and 1.405 maximum. Compared with the other paths, the specimen permeability variation is the largest at the end of the test under composite loading/unloading path, proving that the specimen is more badly damaged under this path.

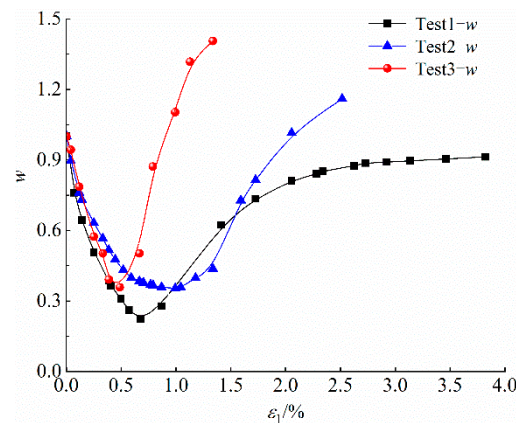


Figure 7. Relative permeability change.

4. Numerical Simulation of Crack Characteristics

In order to examine how cracks in gas-bearing coal evolve under triaxial stress paths, numerical simulations were performed with PFC software to see how crack-count changes in the specimens during loading.

4.1. Model Construction

The model was sized with the same dimensions as the laboratory specimens, i.e., $\phi 50 \text{ mm} \times 100 \text{ mm}$. In the computational model, the minimum particle radius was 0.25 mm, with a particle size ratio of 1.66. A total of 3665 particle samples were generated.

Figure 8 shows the initial and boundary conditions used for simulation. First, the model was loaded with biaxial compression of axial and confining pressure to 6 MPa by the servo mechanism. Then a high-pressure zone with pressure P was set at the top of the model. The fluid field pressure at the bottom of the model was fixed to 0.1 MPa to indicate connecting to atmospheric pressure.

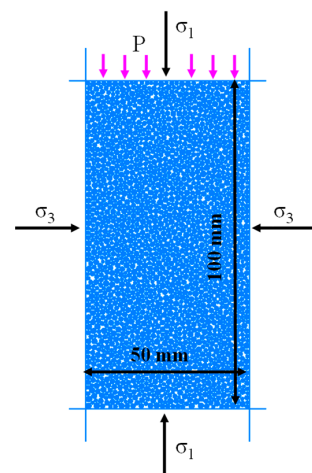


Figure 8. Model, initial conditions and boundary conditions.

4.2. Determination of Coal Meso-Mechanical Parameters

First, coal compression and tension simulations were made with PFC software to correlate the meso- and macro-mechanical parameters of coal.

Data regression yielded a correlation coefficient of 0.992 ($R^2 = 0.992$) between elastic modulus and meso-mechanical parameter, 0.998 ($R^2 = 0.998$) between Poisson's ratio and meso-mechanical parameter, 0.997 ($R^2 = 0.997$) between compressive strength and meso-mechanical parameter, and 0.995 ($R^2 = 0.995$) between tensile strength and meso-mechanical parameter. The empirical equations between these coefficients are shown in Equations (2)–(5).

$$\frac{E}{E_c} = a_1 + b_1 \ln\left(\frac{k_n}{k_s}\right) \quad (2)$$

where E is the elastic modulus, GPa; E_c is the Young's modulus, GPa; k_n/k_s is the stiffness ratio; $a_1 = 1.652$, and $b_1 = -0.395$.

$$\mu = a_2 + b_2 \ln\left(\frac{k_n}{k_s}\right) \quad (3)$$

where μ is the Poisson's ratio; $a_2 = 0.111$; $b_2 = 0.209$.

$$\frac{\sigma_c}{\bar{\sigma}} = \begin{cases} a_3\left(\frac{\bar{\tau}}{\bar{\sigma}}\right)^2 + b_3\frac{\bar{\tau}}{\bar{\sigma}}, & 0 < \frac{\bar{\tau}}{\bar{\sigma}} \leq 1 \\ c_1, & 1 < \frac{\bar{\tau}}{\bar{\sigma}} \end{cases} \quad (4)$$

where σ_c is the compressive strength, MPa; $\bar{\sigma}$ is the parallel connection normal strength, MPa; $\bar{\tau}$ is the parallel connection tangential strength, MPa; $a_3 = -0.965$; $b_3 = 2.292$; and $c_1 = 1.327$.

$$\frac{\sigma_t}{\bar{\sigma}} = \begin{cases} a_4\left(\frac{\bar{\tau}}{\bar{\sigma}}\right)^2 + b_4\frac{\bar{\tau}}{\bar{\sigma}}, & 0 < \frac{\bar{\tau}}{\bar{\sigma}} < 1 \\ c_2, & 1 < \frac{\bar{\tau}}{\bar{\sigma}} \end{cases} \quad (5)$$

where σ_t is the tensile strength, MPa; $a_4 = -0.174$; $b_4 = 0.463$; $c_2 = 0.289$. Based on Equations (2)–(5) and the data in Table 1, the coal mesoscopic parameters required for simulation can be retrieved as shown in Table 2.

Table 1. Macro-mechanical characteristics of the moulded coal specimen.

Bulk Density (kN/m ³)	Elastic Modulus (104 MPa)	Internal Friction Angle (°)	Tensile Strength (MPa)	Cohesion (MPa)	Poisson Ratio
13.57	6.89	42.6	1.34	2.43	0.28

Table 2. Mesoscopic mechanical parameters of the DEM numerical model.

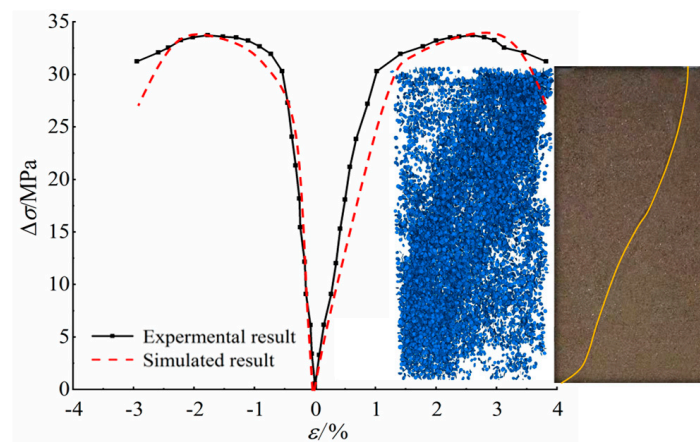
Parameters	Value
Contact stiffness ratio	2.14
Contact modulus (GPa)	5.1
Friction factor	0.4
Parallel bond modulus (GPa)	5.1
Normal strength of parallel bonding	4.6
Parallel bond tangential strength (MPa)	4.6
Parallel bond stiffness ratio	2.14

It has been demonstrated that among all fluid parameters, residual pore size a_0 and fluid viscosity μ make the greatest difference to permeation pressure–stress coupling during permeation. After repeated simulation, fluid computational parameters were worked out, as presented in Table 3.

Table 3. Computational parameters of fluid.

Fluid Viscosity μ /(Pa s)	Fluid Volume Modulus K_f (GPa)	Residual Pore Size a_0 (m)	Initial Normal Stress F_0 (kN)	Time Step Δt (s)
0.015	0.0096	1×10^{-3}	5×10^3	0.1

Figure 9 compares the numerical simulation results with the test results of gas-bearing coal under the stress path of triaxial loading. From this diagram, at the end of the loading path of axial pressure, an oblique shear crack appears in the specimen. The stress-strain curve and failure form from numerical simulation almost entirely agrees with the laboratory test results. This suggests that our numerical simulation model and meso-mechanical parameters are appropriate enough for subsequent meso-mechanical simulation.

**Figure 9.** Comparison of physical test and numerical simulation results.

4.3. Crack Number Characteristic Analysis

To observe crack development inside the specimen under different paths, a cracks count–axial strain plot shown in Figure 10 was drawn. The cracks count inside the specimen changes in much the same way. As axial stress increases, cracks count first increases slowly and then increases quickly, especially near the site of peak stress. Finally, the rate of increase slows down and gradually stabilizes. The evolution of tension and shear-induced cracks count is not much different: it first increases and then stabilizes. However, as tensile strength is greater than shear strength in coal particles, there are many more tensile cracks than shear cracks.

Figure 11 compares the cracks counts at the end of simulation under different paths. In Test 1, the total model cracks count is 4.36×10^3 , including 3.72×10^3 tensile cracks, accounting for 85.29% of total cracks; and 0.64×10^3 shear cracks, accounting for 14.71% of total cracks. In Test 2, the model cracks count is 7.29×10^3 , including 6.05×10^3 cracks, accounting for 82.91% of total cracks; and 1.25×10^3 shear cracks, accounting for 17.09% of total cracks. In Test 3, the model cracks count is 5.65×10^3 , including 4.46×10^3 tensile cracks, accounting for 78.93% of total cracks; and 1.19×10^3 shear cracks, accounting for 21.07% of total cracks. By cracks count, Test 2 > Test 3 > Test 1; by cracks proportion, from Test 1 to Test 3, the proportion of shear cracks gradually increases, suggesting that both tensile cracks and shear cracks are present at the time of failure. For this reason, the model displays a composite tensile–shear failure, although the specimens are more prone to shear failure under loading and composite loading/unloading paths.

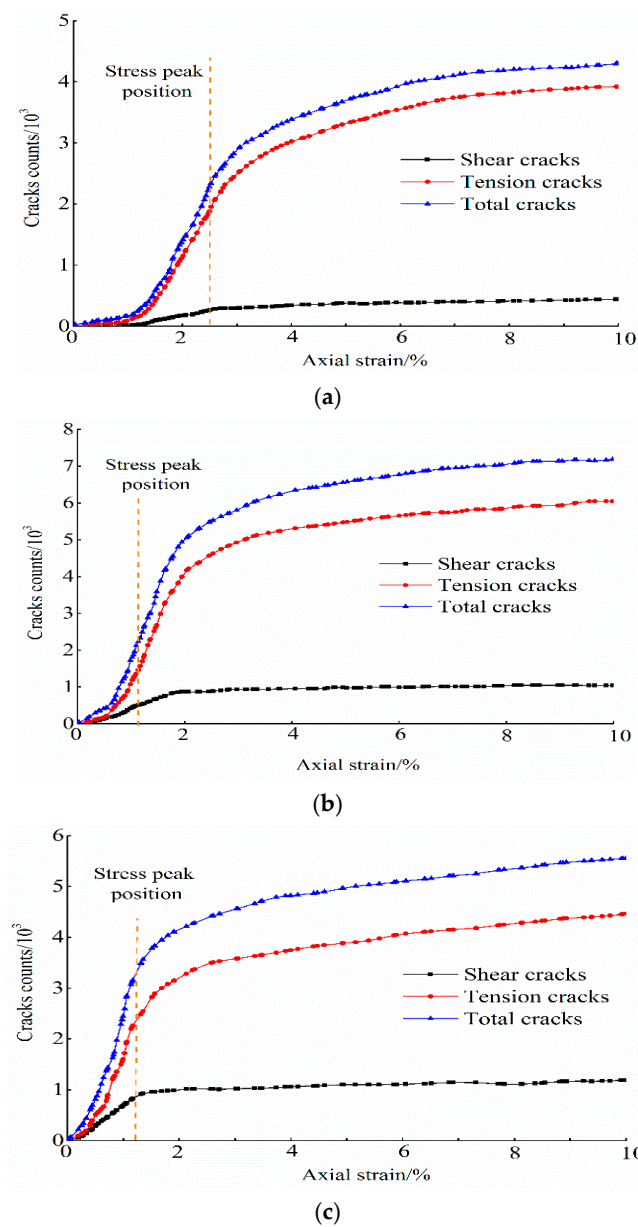


Figure 10. Relationship between the number of cracks and axial strain. (a) Test 1, (b) Test 2, (c) Test 3.

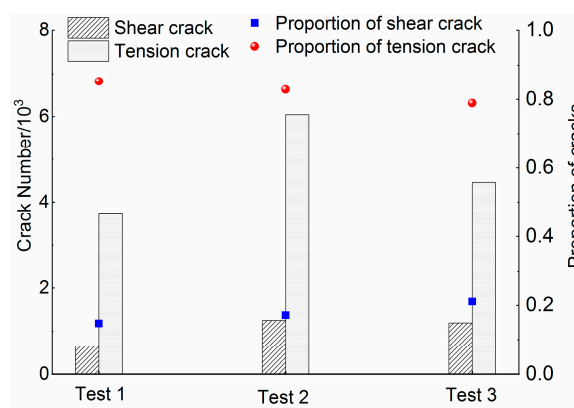


Figure 11. Characteristics of the number of cracks under different paths.

5. Conclusions

In Test 1, the specimen strength is the highest, with $\Delta\sigma = 33.750$ MPa. In Test 2, the specimen strength is the second highest, with $\Delta\sigma = 33.750$ MPa. In Test 3, the specimen strength is the lowest, with $\Delta\sigma = 23.480$ MPa. The specimen-bearing capacity is much lower under loading and composite loading/unloading paths.

Under the three paths, as the test goes on, permeability first reduces then increases; the valley deflection of permeability falls before the peak deflections of the ε_1 - $\Delta\sigma$ curve in all cases. Compared with the other paths, the specimen-permeability variation is the largest at the end of Test 3, proving that the specimens are more badly damaged in Test 3.

The total cracks count is the largest in Test 2. From cracks proportion, from Test 1 to Test 3, the proportion of shear cracks in the model gradually increases, suggesting that both tensile and shear cracks are present at the time of macroscopic failure. For this reason, the model displays a composite tensile–shear failure, although the specimens are more prone to shear failure under loading and composite loading/unloading paths.

Author Contributions: Conceptualization, H.S. (Haibo Sun), B.Z., Z.S., B.S. and H.S. (Hongyu Song); Writing—original draft, H.S. (Haibo Sun); Funding acquisition, B.Z.; Formal analysis, H.S. (Haibo Sun), B.Z. and Z.S.; Software, H.S. (Haibo Sun), B.S.; Data curation, H.S. (Haibo Sun), B.Z. and H.S. (Hongyu Song). All authors have read and agreed to the published version of the manuscript.

Funding: This research received no external funding.

Data Availability Statement: All relevant data presented in the article are according to institutional requirements and, as such, are not available online. However, all data used in this manuscript can be made available upon request to the authors.

Conflicts of Interest: The authors declare no conflict of interest.

References

- Xie, H.; Gao, M.; Zhang, R. Study on the mechanical properties and mechanical response of coal mining at 1000 m or deeper. *Rock Mech. Rock Eng.* **2019**, *52*, 1475–1490. [[CrossRef](#)]
- Yuan, L. Control of coal and gas outbursts in Huainan mines in China: A review. *J. Rock Mech. Geotech. Eng.* **2016**, *8*, 559–567. [[CrossRef](#)]
- Wang, K.; Guo, Y.; Wang, G.; Du, F. Seepage and Mechanical Failure Characteristics of Gas-bearing Composite Coal-Rock under True Triaxial Path. *J. China Coal Soc.* **2022**.
- Zhang, C.; Xu, J.; Peng, S. Dynamic behavior of gas pressure and optimization of borehole length in stress relaxation zone during coalbed methane production. *Fuel* **2018**, *233*, 816–824. [[CrossRef](#)]
- Wang, K.; Du, F.; Zhang, X.; Wang, L.; Xin, C. Mechanical properties and permeability evolution in gas-bearing coal-rock combination body under triaxial conditions. *Environ. Earth Sci.* **2017**, *76*, 815. [[CrossRef](#)]
- Du, F.; Wang, K.; Zhang, X. Experimental study of coal-gas outburst: Insights from coal-rock structure, gas pressure and adsorptivity. *Nat. Resour. Res.* **2020**, *29*, 2481–2493. [[CrossRef](#)]
- Du, F.; Wang, K. Unstable failure of gas-bearing coal-rock combination bodies: Insights from physical experiments and numerical simulations. *Process Saf. Environ. Prot.* **2019**, *129*, 264–279. [[CrossRef](#)]
- Chen, Y.; Xu, J.; Peng, S.; Zhang, Q.; Chen, C. Strain localisation and seepage characteristics of rock under triaxial compression by 3D digital image correlation. *Int. J. Rock Mech. Min. Sci.* **2022**, *152*, 105064. [[CrossRef](#)]
- Chen, C.; Xu, J.; Okubo, S.; Peng, S. Damage evolution of tuff under cyclic tension–compression loading based on 3D digital image correlation. *Eng. Geol.* **2020**, *275*, 105736. [[CrossRef](#)]
- Yin, G.; Li, W.; Li, M. Experimental study of mechanical properties of coal containing methane under different loading-unloading conditions. *Chin. J. Rock Mech. Eng.* **2013**, *32*, 892–901.
- Wang, Y.; Xie, H.; Chen, S. Petrophysical and Mechanical Properties of Complex Structure Coalbed Methane Reservoir: A Laboratory Investigation. *Rock Mech. Rock Eng.* **2022**, 1–19. [[CrossRef](#)]
- Zhao, H.; Wang, J. Experimental study of evolution law of mechanical properties of coal containing gas under unloading confining Pressure. *Rock Soil Mech.* **2011**, *32* (Suppl. S1), 270–274.
- Wang, G.; Xue, D.; Gao, H. Study on permeability characteristics of coal rock in complete stress-strain process. *J. China Coal Soc.* **2012**, *37*, 107–112.
- Li, X.; Yin, G.; Cai, B. Experimental study on deformation and seepage properties of outburst coal samples under cyclic loading. *Chin. J. Rock Mech. Eng.* **2010**, *29* (Suppl. S2), 3498–3504.
- Cao, S.; Bai, Y.; Li, Y. Experiments of coal's gas seepage with outburst dangers. *J. Chongqing Univ.* **2011**, *34*, 91–95.

16. Xue, D.; Zhou, H.; Wang, Z. Failure mechanism and mining-induced mechanism of coal a under different loading rates. *J. China Coal Soc.* **2016**, *41*, 595–602.
17. Chaudry, M.A.; Wriggers, P. On the computational aspects of comminution in discrete element method. *Comput. Part. Mech.* **2018**, *5*, 175–189. [[CrossRef](#)]
18. Zhu, F.; Zhao, J. A peridynamic investigation on crushing of sand particles. *Geotechnique* **2019**, *69*, 526–540. [[CrossRef](#)]
19. Tan, X.; Hu, Z.; Cao, M.; Chen, C. 3D discrete element simulation of a geotextileencased stone column under uniaxial compression testing. *Comput. Geotech.* **2020**, *126*, 103769. [[CrossRef](#)]
20. Indraratna, I.; Thakur, P.; Vinod, J.S. Experimental and numerical study of railway ballast behavior under cyclic loading. *Int. J. Geomech.* **2010**, *10*, 136–144. [[CrossRef](#)]
21. Wang, P. Study of the borehole hydraulic fracturing and the principle of gas seepage in the coal seam. *Procedia Earth Planet. Sci.* **2009**, *1*, 1561–1573.
22. Jiang, M.; Zhang, F.; Sun, Y. An evaluation on the degradation evolutions in three constitutive models for bonded geomaterials by DEM analyses. *Comput. Geotech.* **2014**, *57*, 1–16. [[CrossRef](#)]
23. Ismai, Y.; Yang, D.; Ye, J. A DEM model for visualising damage evolution and predicting failure envelope of composite laminae under biaxial loads. *Compos. Part B Eng.* **2016**, *10*, 9–28. [[CrossRef](#)]
24. Yang, X.; Jing, H.; Chen, K. Numerical simulations of failure behavior around a circular opening in a non-persistently jointed rock mass under biaxial compression. *Int. J. Min. Sci. Technol.* **2016**, *26*, 729–738. [[CrossRef](#)]
25. Sagong, M.; Park, D.; Yoo, J.; Lee, J. Experimental and numerical analyses of an opening in a jointed rock mass under biaxial compression. *Int. J. Rock Mech. Min. Sci.* **2011**, *48*, 1055–1067. [[CrossRef](#)]
26. Raisianzadeh, J.; Mirghasemi, A.A.; Mohammadi, S. 2D simulation of breakage of angular particles using combined DEM and XFEM. *Powder Technol.* **2018**, *336*, 282–297. [[CrossRef](#)]
27. Xu, H.; Qin, Y.; Wang, G.; Fan, C.; Wu, M.; Wang, R. Discrete element study on mesomechanical behavior of crack propagation in coal samples with two prefabricated fissures under biaxial compression. *Powder Technol.* **2020**, *375*, 42–59. [[CrossRef](#)]
28. Wang, G.; Guo, Y.; Wang, P. A new experimental apparatus for sudden unloading of gas-bearing coal. *Bull. Eng. Geol. Environ.* **2020**, *79*, 857–868. [[CrossRef](#)]
29. Zhao, Y.; Cui, D.; Liu, J.; Wei, M.; Liu, Y. Evolution of Coal Permeability under Constant Effective Stresses: Direct Measurements and Numerical Modeling. *Energy Fuels* **2021**, *35*, 15489–15501. [[CrossRef](#)]